ADVANCED QUANTUM TECHNOLOGIES
www.advquantumtech.com

2 µm Ghost Spectroscopy with an Integrated Silicon Quantum Photonics Source

*Matteo Sanna, Davide Rizzotti, Stefano Signorini, and Lorenzo Pavesi**

A ghost spectroscopy measurement with an entangled photon source is demonstrated. The transmission spectrum at the 2 µm absorption peak of gaseous carbon dioxide (CO_2) is measured in a highly noisy environment. Despite the noise, a high sensitivity $S = (5.7 \pm 0.1) \times 10^{-2}$ $(g/l)^{-1}$ is obtained, a value that is larger than the one found for a classical spectroscopy measurement performed in the same conditions. The probe photons are time-energy correlated photon pairs generated through intermodal spontaneous four-wave mixing in a silicon waveguide. This observation opens the way to low-cost on-chip MIR sensors insensitive to environmental noise.

1. Introduction

Photon pair sources are at the basis of many quantum applications, ranging from quantum computing[1,2] and communication,[3] to sensing[4] and imaging.[5] Typically, quantum photonic applications focus on degenerate or moderately non-degenerate correlated photon pairs (a wavelength separation $\lesssim 100$ nm between the photons). However, extremely non-degenerate generation ($\gtrsim 500$ nm) can be a unique resource with intriguing applications. This is the case when dealing with gas spectroscopy, where one would like to exploit simultaneously the advantages of two different spectral regions: on the one hand, mid-infrared (MIR) photons are needed to probe the strong and unique MIR fingerprint absorption lines of gases,[6] while, on the other hand, infrared (IR), or visible (VIS) photons are preferred because of the more mature and efficient detection and spectroscopy technologies.[7–9] A way to exploit both the advantages is by means of ghost spectroscopy (GS), also known as correlated photon spectroscopy.[10,11] The basic idea of GS is to use correlated photon pairs, where one photon of the pair probes the sample and triggers the spectral analysis of the other. The first advantage with respect to traditional absorption spectroscopy is to time filter the events not in coincidence, reducing the overall background noise.[12] This is especially useful when dealing with highly noisy environments, where the noise is unknown and changes during the measurement. In this case, GS outperforms traditional absorption spectroscopy.[13] A second advantage is related to the energy correlation between the paired photons, which gives the possibility to move the spectral analysis at wavelengths where optical technologies (e.g., monochromators, detectors, filters...) are less expensive and more efficient. In fact, thanks to energy correlation, the spectrum probed by one of the photons in the pair, is "mirrored" at the wavelengths where the other one is analyzed. Moreover, any action on the heralding photon, such as spectral filtering, will reflect on the other one. Finally, if the source is operated at the single photon level, sub shot-noise-limit (SNL) measurements are possible. This is also appealing to reduce illumination effects in samples, which are highly sensitive to light intensity.[14] The idea of exploiting correlations for quantum-improved transmission measurements dates back to 1986.[15] The first experimental demonstration arrived in 1995 with the first ghost imaging (GI) measurement.[16] Subsequently, pair-based quantum sensing and imaging experiments, like GS, GI, and undetected photon measurements, have been extensively investigated. For the generation of photon pairs, most works rely on spontaneous parametric down-conversion (SPDC) in bulk or poled crystals[17] sources. Second order nonlinear optical crystals have high generation efficiency and allow broadband generation.[18] However, these depend critically on alignment and temperature, both for stability and for tuning the generated wavelength. An alternative has been proposed by using spontaneous four-wave mixing (SFWM) in a birefringent fiber, that has been applied to GS between VIS and IR.[12] Fiber-based solutions offer robustness and low costs. Moreover, being based on SFWM, just by moving the wavelength of the pump, the generated wavelengths can be easily tuned, resulting in an easier spectral measurement. Even higher robustness and lower costs would be possible with silicon photonics. However, until now, GS or GI have never been demonstrated on this platform. On-chip GS would enable even lower costs and footprints than the fiber counterpart, with potentially higher efficiency. Demonstrating a fully integrated device able to perform GS on a miniaturized chip would open the way to the development of low-cost, robust, and compact sensors for medical diagnostics, air

M. Sanna, D. Rizzotti, S. Signorini, L. Pavesi
Nanoscience Laboratory, Department of Physics
University of Trento
Via Sommarive 14, Trento 38123, Italy
E-mail: lorenzo.pavesi@unitn.it
D. Rizzotti, S. Signorini
ICFO-Institut de Ciencies Fotoniques
Castelldefels, Barcelona 08860, Spain

The ORCID identification number(s) for the author(s) of this article can be found under https://doi.org/10.1002/qute.202300159

DOI: 10.1002/qute.202300159

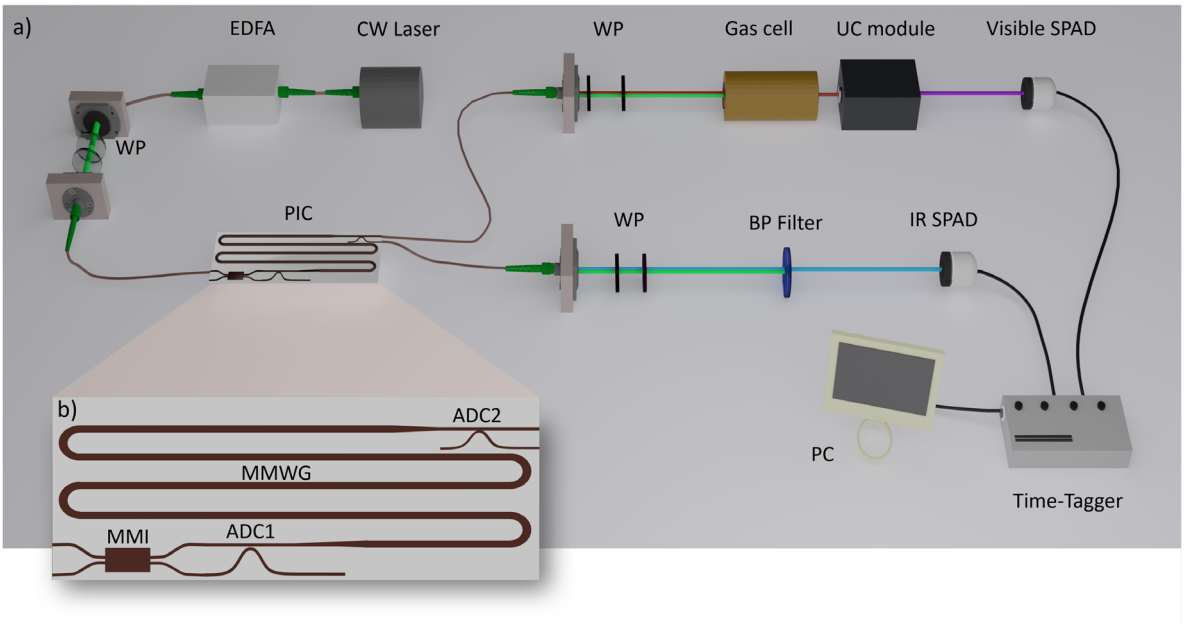

Figure 1. a) The scheme of the experimental setup. A pump beam generated by a tunable continuous-wave (CW) laser is amplified through an erbium-doped fiber amplifier (EDFA) and filtered through a band-pass filter (BPF) to remove the amplified spontaneous emission (ASE) produced by the EDFA. Wave-plates are used to adjust the polarization. Light is coupled to the chip through edge-coupling using a lensed tapered fiber. The same yields for the output coupling. After the chip, the idler is polarized by means of WPs. Raman and pump photons are rejected through a short-pass filter with the cut-off wavelength at 1337 nm. The idler photons are detected via an InGaAs single photon avalanche diode (SPAD model IDQ-id210). The signal photons, after being polarized, pass through the CO_2 gas cell, after which they are up-converted to the visible by means of the up-conversion module (UC). The up-converted signal is then detected by means of a Silicon SPAD (Excelitas SPCM-AQRH-12). Coincidence counts between the two SPADs are recorded through a time-tagger (time-tagger 20 Swabian Instruments). b) PIC design. On-chip, the pump beam is split by a 3-dB multimode interferometer (MMI). Half of the power propagates through the multimode waveguide (MMWG) on the TE0. The other half is converted to the TE1 mode, through an asymmetric directional coupler (ADC), ADC1 in figure, before entering as well the MMWG. In the MMWG, idler, on the TE0, and signal, on the TE1, are generated through intermodal SFWM. Idler and signal are separated on-chip by means of a second ADC (ADC2) and are out-coupled via two edge-coupled tapered lensed fibers.

monitoring or spectroscopy at large. The fundamental component for such integrated device is the source, whose desirable properties are large detuning from the pump, tunable generation, and high coincidence-to-accidental ratio (CAR). Recently, we demonstrated a photon pair source in silicon able to generate photons beyond 2 μm by means of intermodal SFWM.[19] In the present work, we improve such source in terms of maximum *CAR* (105.8), and we use it to demonstrate a GS measurement based on a photonic integrated circuit (PIC). In particular, we perform GS of carbon dioxide (CO_2), also showing its superior performance with respect to classical approaches when dealing with a highly noisy environment. Referring to photon pair sources beyond 2 μm, our source exhibits the best performance for integrated sources[20] and it is close to the best poled crystals solutions.[21] The paper is organized as follows: in Section 2 the source is presented and characterized, while in Section 3 the results of the GS measurement of the CO_2 spectrum around 2 μm are shown. Section 4 concludes the paper.

2. Photonic Integrated Circuit Design and Characterization

The source is based on intermodal SFWM in a SOI multimode waveguide.[22] Intermodal phase matching leverages the different effective indices of distinct spatial modes to achieve phase matching. We used transverse electric polarization (TE), with one pump photon on the fundamental mode (TE0), the other pump photon on the first excited mode (TE1), the signal photon on TE1, and the idler photon on TE0. We name signal the photon in the pair with higher wavelength, while idler is the lower wavelength one. The multimode waveguide is a channel waveguide 1.5 cm long with 2 μm ×0.220 μm cross-section, which phase-matches signal and idler wavelengths around 2000 and 1290 nm, respectively, with the pump in the L-band. **Figure 1** shows the design of the PIC that was fabricated at IMEC within a MPW run. The low propagation losses 1.8 $dBcm^{-1}$ at 1550 nm allows CW pumping of SFWM unlikely in our previous work.[19] The use of an intermodal process has three main advantages: far detuning from the pump and high non-degeneracy of idler and signal, filter-free narrowband generation, and high tunability of the signal wavelength while keeping the idler almost unchanged.[23,24] These peculiarities enable easy pump and Raman noise rejection, IR-MIR entangled pair generation with easy and broadband tunability of the MIR photon.[19] A detailed description of the setup is provided in Figure 1. To be noticed that to perform the signal detection beyond 2 μm, we convert the signal to visible wavelengths around 690 nm through the same up-converter used in Ref. [19, 25].

In order to characterize the source, a number of parameters have been measured and simulated. The first is the wavelength

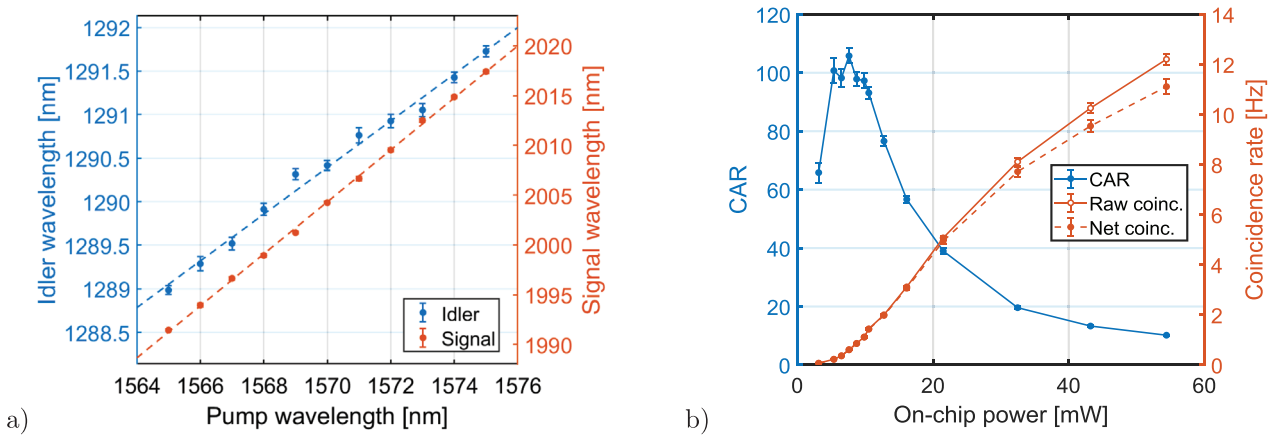

Figure 2. a) Frequency conversion of the SFWM process: in blue the pump-idler conversion, while in orange the pump-signal conversion. The blue points are the measured values (Ten measures per point to estimate the standard deviation), while the red ones are obtained through energy conservation from those of the idler. The dashed lines are linear fits. b) In blue the *CAR* as a function of the on-chip pump power. In orange the raw (void dots) and net (filled dots) coincidence rates as a function of the on-chip pump power. Both the *CAR* and the coincidence rates have been measured with a coincidence bin width of 0.35 ns. The lines are a guide for the eye.

dependence of the generated photons on the pump wavelength, reported in **Figure 2**a. Thanks to energy conservation, it is possible to obtain the signal dependence (in the MIR) by only measuring the idler one (in the NIR). It can be seen that small variations of the pump wavelength (about 12 nm span) correspond to large variations in the MIR region (about 30 nm span), improving what can be achieved by commonly used intramodal FWM.[22,26] We also measured and simulated the spectrum width of the generated photons. The widths remain constant in the range of wavelengths that we considered and are respectively (0.8 ± 0.1) nm for the idler and (1.8 ± 0.3) nm for the signal, see **Figure A2**. As Figure 2a shows, the modes and the waveguide geometry have been chosen in order to generate the signal around the CO_2 absorption peak near 2 μm when pumping in the L-band. This absorption peak has been chosen being free from H_2O absorption lines[27] and because the present source cannot reach wavelengths higher than 2020 nm with the available pump wavelengths ($\leq$ 1575 nm).

Another key parameter to be characterized in a photon pair source is the CAR, reported in Figure 2b. The CAR represents the signal-to-noise ratio of the coincidence measurement. As observed in Figure 2b and in accordance with Equation A14, the CAR is limited at low powers by dark counts and environmental noise and at high power by multi-pair generation. This last limit is due to the fact that the generation of multiple photon pairs gives rise to a higher probability of accidental counts between signal and idlers belonging to different pairs.[28] We measured a fourfold improvement of the *CAR* with respect to the state of the art of silicon sources, compared at the same net coincidence rate of ≈ 1 Hz.[19,20] The maximum *CAR* achieved (105.8 ± 2.5) is more than two times higher with respect to the state of the art in integrated photonics[19] and close to the values reported for $\chi^{(2)}$ crystals.[21]

To complete the characterization of the source, we also measured the heralded second-order coherence function, $g_H^{(2)}$, reported in Section A4, which quantifies how close the source is to single photon behavior.[28]

3. Ghost Spectroscpy Measurements

The time-energy correlation of the photons in the pair provides four concurrent advantages when coming to GS:

1. increased measurement visibility even in low signal-to-noise ratio (SNR) conditions - thanks to the temporal filtering provided by coincidence measurement, which rejects noise counts falling outside the coincidence window;
2. no degradation of the sample - thanks to the fact that GS can operate at the single-photon level while keeping higher visibility of the measurement compared to classical spectroscopy[14];
3. real-time background removal - thanks to the simultaneous monitoring of coincidences and accidentals, that allows also to deal with varying background noises;
4. conversion of the spectral information from the MIR to the IR - this makes the MIR spectral analysis easier.

Therefore, in conditions of high and variable noise, the GS outperforms the standard absorption spectroscopy. This can be shown quantitatively by using Equation (1), where the *SNR* of a classical measurement done with the signal beam and the *CAR* for a GS measurement are compared:

$$SNR = \frac{\rho\eta_s}{\nu_s^M} \qquad CAR = \frac{\eta_i}{\tau(\rho\eta_i + \nu_i^M)} \frac{\rho\eta_s}{\nu_s^M} \tag{1}$$

where $\nu_{s/i}^M$ is the noise rate read by the signal/idler detector, ρ is the generation rate of the source, $\eta_{s/i}$ is the overall transmission efficiency of the system for the signal/idler beam and τ is the temporal window used to count the coincidences. Equation (1) is valid in the low intensity regime (i.e., a mean number of photons $\ll 1$ in a time window τ) and with an unknown noise much greater than the signal itself. Detailed derivation of Equation (1) is reported. Equation (1) shows that, given the same ratio $\rho\eta_s/\nu_s^M$, and considering the typical values of $(\rho\eta_i + \nu_i^M) \simeq 150$ kHz, $\eta_i = 10^{-3}$ and $\tau \simeq 0.35$ ns, the *CAR* improves by a factor of 38 with respect to the *SNR*.

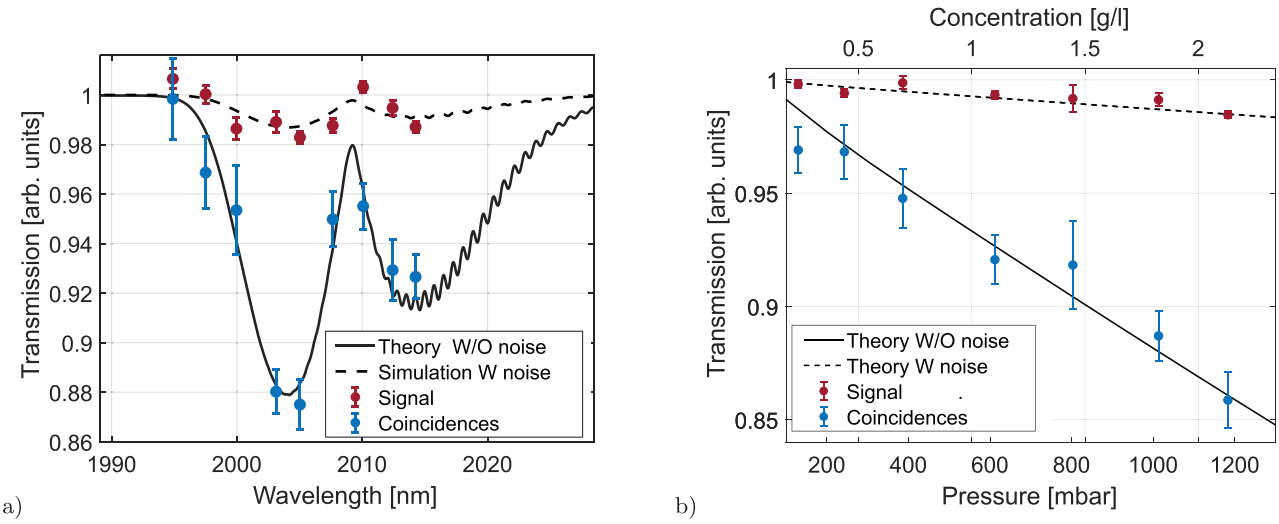

Figure 3. a) Transmission spectra of CO_2 in a cell filled with 1 atm CO_2, measured with both classical absorption spectroscopy done with signal photons counts (red dots) and GS (blue dots). The black lines are the simulated spectra with (dashed line) and without (solid line) noise. The simulations account for the spectral resolution of the system too. b) Transmission through the gas at a fixed wavelength, $\lambda = 2003.3$ nm, as a function of the CO_2 pressure in the gas cell. Both the classical measurement with signal photons (red dots) and the GS measurement (blue dots) are shown. The black lines represent the simulated values for a system with (dashed line) and without (solid line) noise. A time window of $\tau = 1.1$ ns around the center is used.

In Figure 1 the setup used for the GS measurement is reported. By tuning the CW pump wavelength in the range 1565 – 1572 nm, the signal generation covers the spectral range of interest to probe the CO_2 absorption peak around 2 μm (see Figure 2a). We performed two types of measurements, shown in **Figure 3**. In the first, we retrieved the spectrum of CO_2 through GS, and compared it with the spectrum acquired by measuring directly the signal photons transmission. In the second measurement, we fixed the wavelength of the signal and varied the CO_2 pressure in the cell to measure the transmission losses as a function of gas concentration. The procedure to set the pressure (concentration) of CO_2 in the cell, is to first empty the cell down to 0.001 mbar using a rotary pump and, then, flux CO_2 in the cell until the wanted value is reached. A strain gauge is used to monitor the pressure. Even in this second measurement, we compare the result of the GS method with the classical approach. In order to demonstrate the advantage of GS in noisy environments, we increased the background noise in the signal channel through a halogen lamp placed between the upconverter and the visible SPAD. We tuned the lamp in order to decrease the *SNR* from 5.8 to 0.04.

The measurement of the CO_2 transmission spectrum is reported in Figure 3a. Blue dots have been measured through GS via net coincidences. Red dots have been evaluated as the ratio between the unheralded signal counts in the presence and absence of gas. No noise subtraction has been applied, since we wanted to simulate a measurement in real time, without a separate measurement of the noise alone. A reference measurement without gas in the cell is used to normalize the plots.

Each point is calculated from a set of 45 acquisitions of 20 s each. The error bars take into account both the standard deviation and the reference measurement error. In the same graph (Figure 3a), the simulated CO_2 transmission in presence (dashed line) and absence of noise (solid line) is reported. They are calculated as the convolution between the CO_2 spectrum from Hitran[29] and the signal spectrum in absence of noise. It is evident how the GS points (blue dots), despite the noisy environment, are compatible with the expected CO_2 transmission without noise. This means that, in our conditions ($SNR = 0.04$), GS is not affected by the environmental noise within the measurement error. This is not the case for the unheralded measurement (red points), i.e., the standard absorption spectroscopy, which is compatible only with the simulated spectrum taking into account the background noise (dashed line).

In Figure 3b the transmission as a function of the pressure of the gas at a fixed wavelength, $\lambda = 2003.3$ nm, is shown. The wavelength has been chosen to maximize the absorption from the gas. While the GS measurements (blue dots) are compatible with the theoretical values expected in the absence of noise (solid line), the unheralded measurements (red points) match with the model that accounts for noise (dashed line). As a consequence, in a real-world scenario, the GS measurement can retrieve the gas concentration even at low *SNR*s, while the classical one struggles. To compare quantitatively the GS and the classical sensing, we calculated the sensitivity (S) and the limit of detection (LOD) in both cases. These parameters are defined as[30]

$$S = -\frac{\partial T}{\partial C} \quad LOD = \frac{3\sigma}{|S|} \tag{2}$$

where T is the measured transmission for the classical and GS measurement, C is the CO_2 gas concentration related to its pressure and expressed in g l^{-1}, and σ is the standard deviation of the data. These two parameters can be calculated through a linear fit of the curves in Figure 3b. The results are shown in **Table 1**.

The sensitivity of the GS measurement is almost an order of magnitude better than in the classical measurement. However, due to the lower coincidence rate of GS compared to the detection rate of the classical experiment, the GS exhibits poorer measurement statistics and thus higher uncertainty compared

Table 1. Sensitivity, *S*, and limit of detection, *LOD*, values for conventional and ghost spectroscopy measurements generated from Figure 3b.

	Ghost spectroscopy	Classical spectroscopy
S [l g^{-1}]	$(5.7 \pm 0.1) \times 10^{-2}$	$(5.9 \pm 0.1) \times 10^{-3}$
LOD [g l^{-1}]	$(6.7 \pm 1.8) \times 10^{-1}$	(1.3 ± 0.84)

to its classical counterpart. As a result, the *LOD* of GS is only slightly improved with respect to the classical case. The better *LOD* proves that, given the same background noise, coincidence-based sensing allows measuring smaller variations in the concentration with respect to the classical approach. This advantage can be further improved by optimizing the losses on the idler channel, which results in increased coincidences while keeping the signal rate (i.e., the corresponding classical rate) constant. Note that with the classical approach it would be possible to recover the same *S* and *LOD* as with GS, but at the price of a higher illumination intensity, which is needed to overcome the effect of the background noise.

A further advantage of GS is the possibility to increase the resolution of the measurement without the use of MIR equipment. This is possible by narrowing the idler bandwidth through filtering. Indeed, as a consequence of the energy correlation of the photon pair, the effect on the coincidence count is the same as filtering the signal.[31] Another way to increase the resolution is through the use of a longer multimode waveguide source. The longer the waveguide, the narrower the generation spectrum,[22] resulting in higher spectral resolution. *S* and *LOD* can be improved too, by probing an absorption peak with higher cross-section (e.g., for CO_2 around 4.3 μm). This clearly requires a new source that reaches phase matching at this wavelength. It can be achieved by engineering the mode dispersions, e.g., by changing the waveguide cross-section or the spatial modes involved in the process. In Appendix, we propose a new integrated device for the GS of CO_2 at 4.3 μm (**Figure A4 b**). Another way to further improve *LOD* is to decrease σ, that is closely related to the relative error on the measurements. A model of this parameter is presented in the Appendix (see Equation A16), where we show how it depends on critical parameters of the system, such as losses and the time window τ.

4. Conclusion

In this paper, we used an integrated silicon source of photon pairs to demonstrate ghost spectroscopy beyond 2 μm. We probed the CO_2 absorption spectrum and concentration in low *SNR* conditions, demonstrating the advantage of ghost spectroscopy over classical measurement. Particular advantage is seen when the background noise cannot be known a priori. The integrated source, based on intermodal SFWM, shows performances that surpass the state-of-the-art for silicon sources beyond 2 μm. Moreover, intermodal SFWM is ideal for spectroscopy, thanks to the unique spectral tunability of the generated photons. This work is a proof-of-concept of gas spectroscopy, but the same measurement and source can be applied to all those applications requiring high visibility and device compactness. Our result paves the way for fully integrated quantum sensors, which can challenge the current classical devices in terms of performance and costs. Our device can work at room temperature, it is extremely compact and robust, and has the advantage to be tunable and narrow band in the probing spectrum, making it much more selective and specific with respect to state-of-the-art miniaturized sensors (e.g. semiconductor metal oxide sensors).

Appendix A

A.1. Improvement of Coincidence Counting

Here, we show how to extract the theoretical *SNR*s and relative errors on measurements done both with quantum ghost spectroscopy and conventional spectroscopy. In the latter case, unlike in the main text, we consider a situation in which it is possible to measure and subtract the noise from the classical measurement. In this way, we can quantitatively estimate the improvement of our device with respect to a similar classical one.

Assumption and Basic Parameters

We assume a Poisson distributed beam generated by the chip and a constant thermal background noise that is also Poisson distributed, with rates ρ and ν, respectively. η indicates the system efficiency, which includes the detector efficiency and the transmission losses of the system (gas absorption included). The noise is assumed to be generated before the chip and co-propagating with the generated beam. The assumption does not reflect the experiment, where the majority of the noise comes from the halogen lamp after the chip; however, it simplifies the calculations while not changing the results. This is due to the fact that noise is classical light and, so, it does not change its statistics when it experiences losses. Eventually, we will drop this assumption and rewrite the results with ν^M, defined as the measured noise at the detectors.

In order to perform the calculations we need few basic results from the theory of Poisson distributions. Considering a rate ρ and a time window τ, both the mean value and the variance of the distribution are equal to $\rho\tau$. Moreover, the probability of having zero photons in the time window is equal to

$$P(0) = e^{-\rho\tau} \tag{A1}$$

Another fundamental parameter for the calculations is the probability of detecting *n* photons using a bucket detector of efficiency η[32]:

$$P_D(n) = 1 - (1-\eta)^n \xrightarrow[\eta \ll 1]{} n\eta \tag{A2}$$

Parameters of Interests

We want to show a quantitative comparison between the GS measurement and the classical one. To do so, we calculate two parameters: the *SNR* (also called *CAR* when speaking about coincidence measurements) and the relative error on the transmission measurement. By comparing the *CAR* with the *SNR*, we quantify the improvement provided by GS with respect to the classical approach in terms of visibility of the measurement, given a certain amount of background noise. The relative error allows to understand how GS can positively impact the error on the spectral measurement, even when the absolute number of counts is much smaller compared to the classical method.

Conventional Spectroscopy

In this type of measurement the noise cannot be measured simultaneously with the signal. An independent measurement must be acquired in order to be able to subtract it from the transmission measurement. However,

Table A1. Conventional spectroscopy measurements with a photodiode. η includes the transmission coefficient of the system, that of the gas and the detector efficiency. In the final row, the assumption that $\tilde{\nu}$ and ν have the same statistics is used.

Measurement	Mean	Error (std)
Transmission signal	$\rho\eta + \nu\eta$	$\sqrt{\frac{\rho\eta}{T} + \frac{\nu\eta}{T}}$
Noise	$\tilde{\nu}\eta = \nu\eta$	$\sqrt{\frac{\tilde{\nu}\eta}{T}}$
Transmission signal - Noise	$\rho\eta$	$\sqrt{\frac{\rho\eta}{T} + 2\frac{\nu\eta}{T}}$

this is possible only if the noise remains constant during both measurements. We need to distinguish between the noise measured without the signal, $\tilde{\nu}$, and the actual noise present during the signal measurement, ν. Note that the two noise measurements are uncorrelated and, in general, different. However, in the calculations we assume $\tilde{\nu}$ and ν to have the same statistics, so that we can remove the contribution of the noise from the transmission measurement.

When performing spectroscopy with intense light, photodiodes (PDs) are typically used. These devices are sensitive to the number of photons impinging on the detector, hence their behavior differs from that of bucket detectors (see the end of the paragraph for this case). For PDs, the measurement is done averaging the output signal over a time T. In **Table** A1 we show the measurements (first two rows) and the calculated final result (final row), with their respective errors. The final row is calculated as the difference between the first and second row and by propagating the errors.

From the values in Table A1 we can calculate the *SNR* and relative error on the final result:

$$SNR = \frac{\rho}{\nu} \tag{A3}$$

$$\sigma_{rel,cl} = \sqrt{\frac{1}{T}}\sqrt{\frac{1}{\rho\eta}\left(1 + 2\frac{\nu}{\rho}\right)} \xrightarrow[T\to\infty]{} 0 \tag{A4}$$

The limit is for long integration times and represents the best case scenario for this type of measurements. Note that neither the *SNR* and the relative error depend on the integration time in this limit.

Let us now discuss the case in which the detection is made with a bucket detector, as in our experiment. The detector is now insensitive to the number of photons and the counting mechanism gives a binomial distribution to the measurement: either the detector clicks or not. This modifies the statistics of the measurements as described in the next paragraph in Equation A15, but under certain assumptions it yields the same result as Equation A3 and Equation A4. For the sake of clarity, all the approximations used to reach this result are presented in the next paragraph.

Quantum Ghost Spectroscopy

Let us introduce the coincidence time window τ. Its definition relies on the coincidence counting mechanism. If both the idler and signal detectors click within a time window τ we measure that event as a coincidence, otherwise not. All the calculations will be based on the statistics within this time frame. Therefore, we introduce the mean number of photons within the time window τ coming from the generated beam, r, and from the noise, n. These are calculated starting from the rates as

$$r = \rho\tau \qquad n = \nu\tau \tag{A5}$$

Using these parameters, it is possible to write the probability that a single bucket detector, with finite efficiency η, clicks in a time window τ when both the processes are present. The formula and its limit reads[32]:

$$P_{click} = 1 - e^{-(r+n)\eta} \xrightarrow[r\eta, n\eta \ll 1]{} (r+n)\eta + \frac{(r\eta + n\eta)^2}{2} \tag{A6}$$

The limit in Equation A6 represents the single photon regime and it is the Taylor expansion to the second order.

Let us now calculate two probabilities: the one for an accidental count, P_{acc}, and that of coincidence counts, P_{cc}. The former is defined as the probability that the signal detector clicks after a time $|\Delta t| > \tau/2$ with respect to the idler detector. The latter, instead, is the probability that the detectors click at the same time (or better, in the same time window), $|\Delta t| \leq \tau/2$. Since we are interested in the coincidences between the time-correlated photon pairs, the accidental coincidences play the role of noise as the calculations will show. Note that, from now on, we use the subscripts s and i to indicate the signal and idler, respectively.

Accidental counts probability is given by the product of three probabilities: probability that the idler detector clicks within a time τ, probability that the signal detector does not click for a time $|\Delta t| > \tau/2$ (without loss of generality, $\Delta t > 0$) and probability that the signal detector clicks within a time τ. The first and third terms are given by Equation A6. For the second one, we must define $\tilde{r} = \rho\Delta t$ and $\tilde{n} = \nu_s\Delta t$ and the result is [32]:

$$P_{NOclick}(\Delta t) = e^{-(\tilde{r}+\tilde{n})\eta} \xrightarrow[\tilde{r}\eta, \tilde{n}\eta \ll 1]{} 1 - (\tilde{r}+\tilde{n})\eta + \frac{(\tilde{r}\eta + \tilde{n}\eta)^2}{2} \tag{A7}$$

Since the photon-pair generation probability is typically very low, the nonzero order terms in Equation A7 are negligible, meaning that the probability of reading a photon in a time interval Δt is very low. In formula, this reads $\tilde{r}\eta$, $\tilde{n}\eta \ll 1$ and it also implies $r\eta$, $n_i\eta_i$, $n_s\eta_s \ll 1$ (since $\Delta t > \tau/2$). Therefore, the probability of an accidental count is:

$$P_{acc} = \left(1 - e^{-(r+n_i)\eta_i}\right)\left(e^{-(\tilde{r}+\tilde{n}_s)\eta_s}\right)\left(1 - e^{-(r+n_s)\eta_s}\right) \xrightarrow[r\eta, n_i\eta_i, n_s\eta \ll 1]{} (r+n_i)\eta_i(r+n_s)\eta_s \tag{A8}$$

Let us now calculate the probability of coincidences at time $\Delta t = 0$, i.e. within the same time window τ. There are four different events that generate a coincidence. The best way to proceed is to calculate this probability as one minus the probability of not having a click. In turn, this probability is easily calculated as the product of the probabilities of not having a coincidence from any of the four events. The events are: 1) coincidence between the generated idler and signal photons (P_1), 2) coincidence of a generated idler and a noise signal (P_2), 3) coincidence of noise idler and a generated signal (P_3) and 4) coincidence between two noise photons (P_4)[33]. The probability of **not** having these events are:

$$\begin{aligned} P_1 &= e^{-r\eta_s} + e^{-r\eta_i} - e^{r\eta_s\eta_i - r\eta_s - r\eta_i} \\ P_2 &= e^{-r\eta_i} + e^{-n_s\eta_s} - e^{-r\eta_i - n_s\eta_s} \\ P_3 &= e^{-r\eta_s} + e^{-n_i\eta_i} - e^{-r\eta_s - n_i\eta_i} \\ P_4 &= e^{-n_i\eta_i} + e^{-n_s\eta_s} - e^{-n_i\eta_i - n_s\eta_s} \end{aligned} \tag{A9}$$

Hence, after applying the assumption of low intensity regime, the final result yields:

$$P_{cc} = 1 - P_1P_2P_3P_4 \xrightarrow[r\eta, n_i\eta_i, n_s\eta \ll 1]{} r\eta_s\eta_i + r^2\eta_s\eta_i\left[\frac{1}{2}\eta_s\eta_i - (\eta_s + \eta_i)\right] + P_{acc} \tag{A10}$$

The result is composed of three terms: the first one is proportional to η_s, thus also to the losses induced by the gas. Hence, if isolated, it represents a simple way to recover the spectrum of the gas. The third one is identical to P_{acc}, hence it can be measured independently and simultaneously, as shown in Equation A8. Finally, the second term has a nonlinear dependence from the losses induced by the gas, hence, if present, it poses difficulties on retrieving spectral information. Then, let us introduce another assumption: η_s, $\eta_i \ll 1$, that is satisfied by our system. Under all the

assumptions made so far, we can conclude that the second term becomes negligible with respect to the first one and so P_{cc} can be written as:

$$P_{cc} \simeq r\eta_s\eta_i + P_{acc} \tag{A11}$$

Let us now connect this theory to the measurements. The calculated probabilities are valid for a time window τ. We can define $M = T/\tau$ to link the measurement time T to the time window τ. If we add the assumption that each time window is independent to one another, that means that a click in a certain time window does not affect the probability of having a click in any other time window,[34] we can relate the counts N, and so the rate R, to the probabilities:

$$N_{acc} = P_{acc} \cdot M \Rightarrow R_{acc} = \frac{P_{acc}}{\tau} \tag{A12}$$

$$N_{cc} = P_{cc} \cdot M \Rightarrow R_{cc} = \frac{P_{cc}}{\tau} \tag{A13}$$

From these equations, the signal to noise ratio, also called coincidence to accidental ratio (CAR) in this case, is:

$$CAR = \frac{R_{cc} - R_{acc}}{R_{acc}} = \frac{1}{\tau}\frac{\rho}{(\rho + \nu_s)(\rho + \nu_i)} \tag{A14}$$

A key feature of this equation is its dependence from the time window τ: the smaller it is, the higher *CAR* we get. This is what in the paper we call "temporal filtering" of the noisy counts. It happens because the signal/idler counts that generate a coincidence that brings information of the gas spectrum happen simultaneously,[35] while the accidental counts are spread uniformly over all possible delays Δt. Hence, if one infinitely reduces the time window, the noise can be completely eliminated. This is obviously not possible in a real experiment, because of the limited time resolution of the instruments (e.g., time jitter of the detectors, time resolution of the time tagger, ...). However, the formulas does not change, except that the time window has a lower limit. A graphical interpretation of this filtering mechanism is shown in the Section A.2.

Let us now consider the relative error on the final measurement. A count can be seen as a binomial event: either it happens or not. Hence, accidental counts and coincidence counts are binomial distributed with probabilities P_{acc} and P_{cc}, respectively. Moreover, since they are uncorrelated events, error propagation is straightforward. The variance of a binomial distribution is given by:

$$var = MP(1-P) \xrightarrow[P \ll 1]{} MP \tag{A15}$$

where P is either P_{acc} or P_{cc} and the approximation is valid thanks to the assumptions made before. The final measurement is calculated subtracting R_{acc} to R_{cc}, thus its relative error is:

$$\sigma_{rel,qu} = \frac{1}{\sqrt{T}}\sqrt{\frac{1}{\rho\eta_i\eta_s} + 2\frac{\tau}{\eta_i\eta_s}\left(1 + \frac{\nu_i + \nu_s}{\rho} + \frac{\nu_i\nu_s}{\rho^2}\right)} \tag{A16}$$

Note that, as for the classical case, the longer the measurement the better the relative error.

A.1.1. Limit for Very High Signal Noise

Let us discuss more in detail the environment in which the experiment took place. As explained, we made use of a halogen lamp to increase the noise in the signal detector. Hence, this noise does not propagate through the system and can be rewritten by substituting $\nu_{s,i} = \nu_{s,i}^M/\eta_{s,i}$, where the apex stands for "measured". Moreover, in the approximation of very high noise, $\nu_s^M \gg \rho\eta_s$, the *SNR* and *CAR* read:

$$SNR = \frac{\rho\eta_s}{\nu_s^M} \qquad CAR = \frac{\eta_i}{\tau(\rho\eta_i + \nu_i^M)} \cdot \frac{\rho\eta_s}{\nu_s^M} \tag{A17}$$

The difference between *SNR* and *CAR* is represented by the first fraction in the *CAR* equation. This parameter shows that lower losses in the idler channel, smaller time windows and lower idler rates, improve the *CAR* with respect to *SNR*. To be noticed that the former depends also on idler losses and noise. This is expected, since the coincidences depend both on signal and idler rates.

The relative error can be rewritten from Equations A4 and A16 as

$$\sigma_{rel,cl} = \frac{1}{\sqrt{T}}\frac{\sqrt{2\nu_s^M}}{\rho\eta_s} \qquad \sigma_{rel,qu} = \frac{1}{\sqrt{T}}\frac{1}{\sqrt{\rho\eta_s\eta_i}}\sqrt{1 + \frac{2\tau\nu_s^M}{\eta_s}} \tag{A18}$$

Equation A18 shows that the main contribution to the classical error comes from the noise, while the quantum error is the error of a Poisson process plus a correction for noise. From the one hand, the quantum error has the disadvantage of being affected by a much lower number of counts due to the idler losses. On the other hand, the time filter filters out most of the noise contribution to the error. In our conditions, this correction is not negligible, but it can be further improved by decreasing the time window and the losses. As a whole, due to high losses and limits on the time window τ, our system has higher relative errors when performing ghost spectroscopy rather than classical spectroscopy. By substituting typical values under measurement condition we get

$$\frac{\sigma_{rel,qu}}{\sigma_{rel,cl}} \simeq 6 \tag{A19}$$

Even if in our conditions we do not get an advantage from this point of view, Equation A18 is useful to understand which are the parameters that are critical to improve the relative error of the quantum case.

A.2. Temporal Filter Graphical Explanation

Previously we have introduced the concept of "temporal filtering" by discussing coincidence counting. Here, we describe the origin of this name. It is depicted visually in **Figure A1**. The dark blue histogram is the graph of a measurement taken with a standard electrical device data acquisition (Swabian Instruments Time Tagger 20). It represents the coincidence counts as a function of the time delay at which they occur. The spectrum information is all enclosed in the central peak because of the

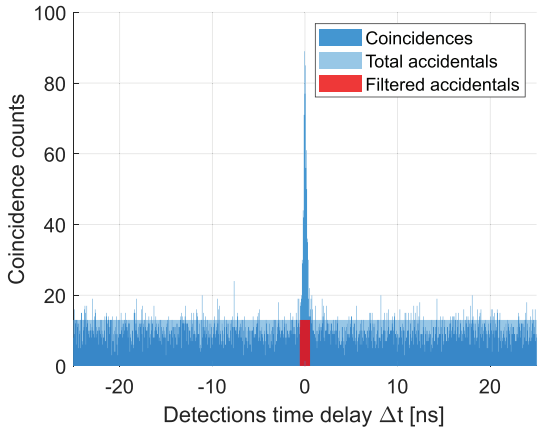

Figure A1. In dark blue a typical data acquisition of coincidence counts from the time tagger device. The instrument records the coincidences as a function of the time delay at which they happen. The time resolution is 50 ps. Two rectangles are superimposed to the measurement: the light blue one shows a portion of the total noisy counts that are present in the system, while in red the only portion of noisy counts considered in GS measurements.

time-correlations of the generated photons. The noisy counts, instead, are spread all over the *x*-axis because they come from uncorrelated sources (light blue rectangle). As a result, we can limit our observations to the counts that occurs during the $\tau = 1.1$ ns window around the center. In this way, the noisy counts are largely filtered while the spectral information is restored (only the ones in the red rectangle remains). This intuitive description is valid under all the assumptions introduced in the previous Section A.1.

A.3. Generated Spectra

In this section, we analyze the spectrum of generated photons. In **Figure A2** a the measured and simulated spectrum of the idler photons when the chip is pumped at $\lambda = 1569$ nm are compared. The measurement is performed under the same pump power levels as when we performed GS (on-chip power of 45 mW) and was done using a custom monochromator with resolution of 2.5 nm. The simulated spectrum comes from the simulation of the JSI of the SFWM process.[28] The simulation matches the experimental graph and predicts a full-width-half-maximum (FWHM) of $\approx$ 0.87 nm for the idler and $\approx$ 2.1 nm for the signal. These widths remain constant over the range of pump wavelength that are used. Figure A2 b shows the simulation of the signal photon spectrum without the influence of the resolution of any instrument. Hence, it is the spectrum of the probe used for the CO_2 spectrum measurement. There are two unbalanced main peaks, surrounded by various smaller peaks that come from the multiple curves on-chip, as explained in ref. [31].

A quantitative measurement of the FWHM of the generated photons further validates the simulation. Since we had just an estimation of the resolution of the monochromator, we performed the measurement by measuring the spectrum of the up-conversion module (that is part of the signal detection stage) both with a MIR laser and with GS (measurement shown in ref. [31]). By propagating the errors, we found a FWHM $= 0.8 \pm 0.1$ nm for the idler photons and FWHM $= 1.8 \pm 0.3$ nm for the signal photons. Both of them are compatible with the shown simulated values.

A.4. Second-Order Coherence Function $g_H^{(2)}$

Information on the photon statistics of the probe state can be retrieved from the second-order coherence function $g^{(2)}(t)$.[28] In particular, $g^{(2)}(0)$ gives a quantitative estimation of how good the single-photon approximation is. Using the signal as the heralded photon and the idler as the herald photon, the single-photon behavior of the source was proved by measuring the heralded $g^{(2)}(0)$ ($g_H^{(2)}(0)$).[19,28] A Hanbury-Brown and Twiss (HBT) interferometer is used in the signal line to carry out this measurement. The value of the $g_H^{(2)}(0)$ as a function of the pump power is shown in **Figure A3**.

By obtaining a minimum $g_H^{(2)}(0) = 0.06 \pm 0.02$ at 10.5 mW, we were able to confirm the anti-bunching regime of the generated photon in the MIR and, hence, the single photon regime of our source.

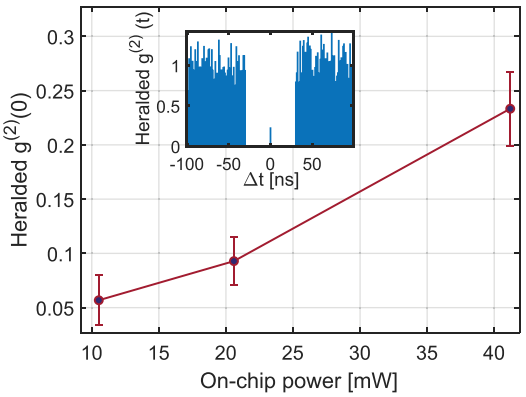

Figure A3. Heralded $g^{(2)}(0)$ as a function of pump power. Measurement for the $g_H^{(2)}(\Delta t)$ at an on-chip power of 10.5 mW is reported in the inset. The adjacent bins to the zero-delayed one have been removed due to the SPAD-emitted photons.

A.5. Ghost Spectroscopy at Longer MIR Wavelengths

In our paper, we demonstrated, as a proof of concept, a GS measurement with one photon around 2 µm. Generating correlated photons with one of them at longer wavelengths would be of great interest for probing the fingerprint of molecules. In this section, we show through a simulation that this scenario is possible by properly engineering the waveguide material and geometry. Let us consider 4.3 µm as our target wavelength for one of the photons in the pair. At this wavelength CO_2 exhibits the highest absorption, allowing for higher detection sensitivity. In order to keep our device cheap and integrable, we consider a pump in the C- or L-band and, so, the idler will be generated in the NIR, around 950 nm. As a consequence, we cannot use silicon as the material for the waveguide, being not transparent at this wavelength. Other materials, such as Silicon Nitride (Si_3N_4)[36] and Silicon Oxynitide (SiON),[37] should be used. For our simulation, we consider Si_3N_4, which exhibits higher nonlinearity and refractive index with respect to SiON. In this case, phase matching reads

$$\begin{cases} \Delta k = k_{p1}^{M_{p1}} + k_{p2}^{M_{p2}} - k_s^{M_s} - k_i^{M_i} \\ k_x^{M_x} = \frac{2\pi}{\lambda_x} n_{eff,x}^{M_x}(\lambda_x) \end{cases} \tag{A20}$$

where $x = p1,\ p2,\ i,\ s$ (pumps, idler, signal), M is the spatial mode, λ is the wavelength, Δk is the phase mismatch and k_i^M is the wavevector of beam x in mode M. According to our simulations, when pump photons are in the fundamental mode (TE0) and idler and signal in the first excited mode (TE1), phase matching can be achieved around 4.3 µm.

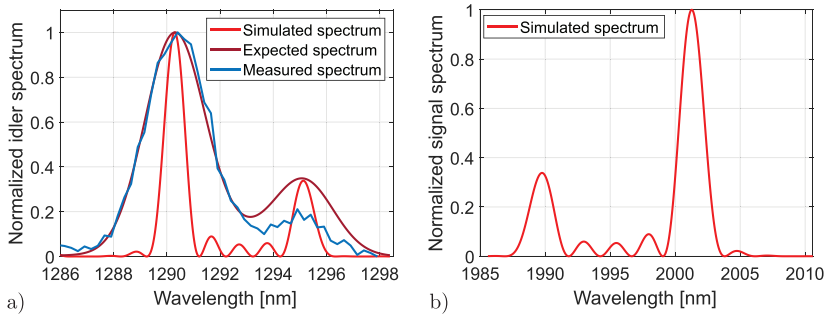

Figure A2. a) Qualitative comparison between a direct measurement of the idler spectrum (blue line) with the simulated spectrum considering the monochromator (dark red line) and not (red lines). The pump wavelength is $\lambda = 1569$ nm. The relative error on each blue point is less than 5%. b) Simulation of the signal photon spectrum without the influence of the resolution of any instrument.

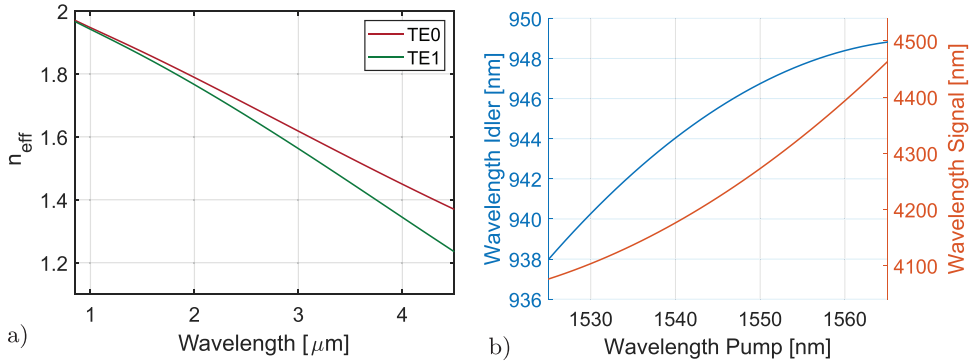

Figure A4. a) Simulated dispersion of the TE0 and TE1 modes in the examined region. The MMWG is a channel waveguide made of Silicon Nitride, (Si_3N_4) , surrounded by air. Dimensions are 6 µm width by 800 nm height. b) Phase matching condition for the intermodal combination TE0, TE0, TE1, TE1 (pump, pump, signal, idler photon, respectively).

We are considering a suspended channel waveguide, to avoid the problem of absorption from silica cladding.[38] A waveguide height of 800 nm is used, a typical value for MIR photonics. The waveguide width that optimizes the generation at the wavelength of interest is 6 µm. **Figure A4** a shows the dispersions of the fundamental mode, TE0, and the first excited mode, TE1, with the waveguide cross-section adopted. In Figure A4 b the generated wavelengths of signal and idler as a function of the pump wavelength are shown.

This simulated result allows to understand the flexibility of the intermodal SFWM source, showing that it is possible to develop an integrated photonic device suitable for MIR quantum photonics and sensing.

Acknowledgements

This project had been supported by Q@TN, the joint lab between University of Trento, FBK- Fondazione Bruno Kessler, INFN-National Institute for Nuclear Physics, and CNR-National Research Council and financed by PAT. Author S.S. had received funding from the European Union's Horizon 2020 research and innovation programme under the Marie Skłodowska-Curie grant agreement no. 754510.

Conflict of Interest

The authors declare no conflict of interest.

Data Availability Statement

The data that support the findings of this study are available from the corresponding author upon reasonable request.

Keywords

four wave mixing, photonic entanglement, photonic integrated circuits, quantum metrology, quantum spectroscopy

Received: May 31, 2023
Revised: September 11, 2023
Published online: October 16, 2023

[1] T. D. Ladd, F. Jelezko, R. Laflamme, Y. Nakamura, C. Monroe, J. L. O'Brien, *nature* **2010**, *464*, 45.
[2] H.-S. Zhong, H. Wang, Y.-H. Deng, M.-C. Chen, L.-C. Peng, Y.-H. Luo, J. Qin, D. Wu, X. Ding, Y. Hu, P. Hu, X.-Y. Yang, W.-J. Zhang, H. Li, Y. Li, X. Jiang, L. Gan, G. Yang, L. You, Z. Wang, L. Li, N.-L. Liu, C.-Y. Lu, J.-W. Pan, *Science* **2020**, *370*, 1460.
[3] N. Gisin, G. Ribordy, W. Tittel, H. Zbinden, *Rev. Mod. Phys.* **2002**, *74*, 145.
[4] J. P. Dowling, *Contemp. Phys.* **2008**, *49*, 125.
[5] G. Brida, M. Genovese, I. R. Berchera, *Nat. Photonics* **2010**, *4*, 227.
[6] J. Hodgkinson, R. P. Tatam, *Meas. Sci. Technol.* **2012**, *24*, 012004.
[7] D. Jung, S. Bank, M. L. Lee, D. Wasserman, *J. Opt.* **2017**, *19*, 123001.
[8] M. Vainio, L. Halonen, *Phys. Chem. Chem. Phys.* **2016**, *18*, 4266.
[9] C. R. Petersen, U. Møller, I. Kubat, B. Zhou, S. Dupont, J. Ramsay, T. Benson, S. Sujecki, N. Abdel-Moneim, Z. Tang, D. Furniss, A. Seddon, O. Bang, *Nat. Photonics* **2014**, *8*, 830.
[10] G. Scarcelli, A. Valencia, S. Gompers, Y. Shih, *Appl. Phys. Lett.* **2003**, *83*, 5560.
[11] P. Janassek, S. Blumenstein, W. Elsäßer, *Opt. Photonics News* **2018**, *29*, 41.
[12] E. Pearce, C. Phillips, R. Oulton, A. Clark, *Appl. Phys. Lett.* **2020**, *117*, 054002.
[13] A. Kalachev, D. Kalashnikov, A. Kalinkin, T. Mitrofanova, A. Shkalikov, V. Samartsev, *Laser Phys. Lett.* **2007**, *4*, 722.
[14] R. Whittaker, C. Erven, A. Neville, M. Berry, J. O'Brien, H. Cable, J. Matthews, *New J. Phys.* **2017**, *19*, 023013.
[15] E. Jakeman, J. Rarity, *Opt. Commun.* **1986**, *59*, 219.
[16] T. B. Pittman, Y. Shih, D. Strekalov, A. V. Sergienko, *Phys. Rev. A* **1995**, *52*, R3429.
[17] D. Strekalov, A. Sergienko, D. Klyshko, Y. Shih, *Phys. Rev. Lett.* **1995**, *74*, 3600.
[18] S. Carrasco, M. B. Nasr, A. V. Sergienko, B. E. Saleh, M. C. Teich, J. P. Torres, L. Torner, *Opt. Lett.* **2006**, *31*, 253.
[19] S. Signorini, M. Sanna, S. Piccione, M. Ghulinyan, P. Tidemand-Lichtenberg, C. Pedersen, L. Pavesi, *APL Photonics* **2021**, *6*, 126103.
[20] L. M. Rosenfeld, D. A. Sulway, G. F. Sinclair, V. Anant, M. G. Thompson, J. G. Rarity, J. W. Silverstone, *Opt. Express* **2020**, *28*, 37092.
[21] S. Prabhakar, T. Shields, A. C. Dada, M. Ebrahim, G. G. Taylor, D. Morozov, K. Erotokritou, S. Miki, M. Yabuno, H. Terai, C. Gawith, M. Kues, L. Caspani, R. H. Hadfield, M. Clerici, *Sci. Adv.* **2020**, *6*, eaay5195.
[22] S. Signorini, M. Mancinelli, M. Borghi, M. Bernard, M. Ghulinyan, G. Pucker, L. Pavesi, *Photonics Res.* **2018**, *6*, 805.
[23] S. Signorini, M. Finazzer, M. Bernard, M. Ghulinyan, G. Pucker, L. Pavesi, *Front. Phys.* **2019**, 128.
[24] S. Paesani, M. Borghi, S. Signorini, A. Maïnos, L. Pavesi, A. Laing, *Nat. Commun.* **2020**, *11*, 1.

[25] M. Mancinelli, A. Trenti, S. Piccione, G. Fontana, J. S. Dam, P. Tidemand-Lichtenberg, C. Pedersen, L. Pavesi, *Nat. Commun.* **2017**, *8*, 1.
[26] S. Signorini, Ph.D. thesis, University of Trento, Trento TN, Italy **2019**.
[27] F. Ottonello-Briano, C. Errando-Herranz, H. Rödjegård, H. Martin, H. Sohlström, K. B. Gylfason, *Opt. Lett.* **2020**, *45*, 109.
[28] S. Signorini, L. Pavesi, *AVS Quantum Sci* **2020**, *2*, 041701.
[29] HITRAN, Hitran website main page, https://hitran.org/ (accessed: June 2021).
[30] A. Shrivastava, V. B. Gupta, *Chron. Young Sci* **2011**, *2*, 21.
[31] M. Sanna, D. Rizzotti, S. Signorini, L. Pavesi, in *Quantum Sensing and Nano Electronics and Photonics XVIII*, Vol. *12009*, SPIE, Bellingham, Washington USA **2022**, pp. 143–151.
[32] C. Silberhorn, *Contemp. Phys.* **2007**, *48*, 143.
[33] In turn, each one of P_1, P_2, P_3 and P_4 are calculated as one minus the probability of having the respective event.
[34] This is not true in reality because of the response time of the system. However, if a proper time window is used, this assumption holds.
[35] It is limited by the bandwidth of the generated photons, and by the time response of the instruments. In our case this last prevails.
[36] T. D. Bucio, C. Lacava, M. Clementi, J. Faneca, I. Skandalos, A. Baldycheva, M. Galli, K. Debnath, P. Petropoulos, F. Gardes, *IEEE J. Sel. Top. Quantum Electron.* **2019**, *26*, 1.
[37] G. Piccoli, M. Sanna, M. Borghi, L. Pavesi, M. Ghulinyan, *Opt. Mater. Express* **2022**, *12*, 3551.
[38] J. S. Penadés, A. Sánchez-Postigo, M. Nedeljkovic, A. Ortega-Moñux, J. Wangüemert-Pérez, Y. Xu, R. Halir, Z. Qu, A. Khokhar, A. Osman, W. Cao, C. G. Littlejohns, P. Cheben, I. Molina-Fernández, G. Z. Mashanovich, *Opt. Lett.* **2018**, *43*, 795.